Manuscript
Click here to download Manuscript: manuscript.docx
Click here to view linked References

The leading modes of decadal SST variability in the Southern Ocean in CMIP5 simulations

Gang Wang* and Dietmar Dommenget

School of Earth, Atmosphere and Environment, Monash University,
Clayton, Victoria, 3800, Australia

Submitted to Climate Dynamics

May 2015

*Corresponding author:
Gang Wang
gang.wang@monash.edu
+61-3-990-24214

ABSTRACT

The leading modes of Sea Surface Temperature (SST) variability in the Southern Ocean on decadal and even larger time scales are analysed using Coupled Model Intercomparison Project 5 (CMIP5) model simulations and observations. The analysis is based on Empirical Orthogonal Function (EOF) modes of the CMIP5 model super ensemble. We compare the modes from the CMIP5 super ensemble against several simple null hypotheses, such as isotropic diffusion (red noise) and a Slab Ocean model, to investigate the sources of decadal variability and the physical processes affecting the characteristics of the modes. The results show three main modes in the Southern Ocean: the first and most dominant mode on interannual to decadal time scales is an annular mode with largest amplitudes in the Pacific, which is strongly related to atmospheric forcing by the Southern Annular Mode (SAM) and El Nino Southern Oscillation (ENSO). The second mode is an almost basin wide monopole pattern, which has pronounced multi-decadal and longer time scales variability. It is firstly inducted by the Wave-3 patterns in the atmosphere and further developed via ocean dynamics. The third mode is a dipole pattern in the southern Pacific that has a pronounced peak in the power spectrum at multi-decadal time scales. All three leading modes found in the CMIP5 super model have distinct patterns and time scale behavior that can not be explained by simple stochastic null hypothesis, thus all three leading modes are ocean-atmospheric coupled modes and are likely to be substantially influenced or driven by ocean dynamical processes.

Key words: CMIP5; Southern Ocean; Climate modes; Decadal variability

1. Introduction

The Southern Ocean (SO), for its large heat and carbon capacity, plays a critical role in the Earth climate system (e.g. Sabine et al. 2004; Séférian et al., 2012). There are evidences that decadal and even longer variability exists in the SO, such as tree rings in Tasmania (Villalba et al, 1997, Cook et al. 2000) and increase of the Antarctic sea ice extent (e.g., Cavalieri and Parkinson 2008; Comiso and Nishio 2008).

However, due mainly to sparse observations, the long-term climate variability of the SO has not been studied extensively especially on the larger scale as its Northern Hemisphere counterpart. For the Sea Surface Temperature (SST) variability, most research focus on the remote response to the El Nino/Southern Oscillation (ENSO) (e.g. Karoly 1989; Kidson and Renwich, 2002; Mantua and Hare, 2002). The Rossby wave teleconnection patterns in the Southern Hemisphere atmosphere, known as the Pacific South America (PSA) patterns, transport the ENSO climate anomalous signals from the tropics to high southern latitudes (e.g. Mo and Higgins, 1998; Renwick, 2002; Turner, 2004). Another important factor in the SO is the Southern Annular Mode (SAM), which could be defined as the leading EOF pattern of sea level pressure (SLP) at 20~70°S and is approximately zonally symmetric, but out of phase between middle and high latitudes (Kidson, 1988; Karoley, 1990; Thompson and Wallace 2000; Jones et al. 2009). The SAM affects the westerly circumpolar flow, then further influence the circulation, temperature distribution, mixed layer depth and heat capacity in the ocean via the Ekman pumping effect (e.g. Fyfe, 2003; Boer et al. 2001; Cai and Watterson, 2002). Recent studies suggest that a quasi-decadal variability exists in the SAM (Yuan and Li, 2008; Yuan and Yonekura, 2011).

Within the deeper subsurface SO, the intrinsic variability is closely related to the Antarctic Circumpolar Current (ACC). The baroclinic instability originates within the thermocline of the ACC (O'Kane et al., 2013), and further results into positive feedbacks between meso-scale eddies and the ACC mean flow (Hogg and Blundell, 2006). On even longer-term variability the Southern Ocean centennial variability is possibly caused by deep ocean overturning circulation changes, as discussed in model based studies (e.g. Latif et.al, 2013).

Further, a number of modes in the atmosphere-ocean system have been identified in the Southern Hemisphere, such as the Trans-Polar Index (TPI, Jones et al, 1999), Antarctic Circumpolar Wave (ACW, e.g. White and Peterson, 1996) and South Pacific subtropical Dipole (Morioka et al., 2013). They might also exhibit decadal variations, which are still unclear.

The length of observation records and limitations of models restrict our understanding of the long-term variability in the Southern Ocean. Besides, most previous studies focus on the modes from the atmosphere rather than from the ocean, mainly because of the relative abundance of the atmospheric data. However, as the significant heat content of the SO, the ocean itself should have more influence on the decadal and even longer variations. In this study presented here we will base our SST variability analyses within SO on the empirical orthogonal function (EOF) modes in the model simulations and observations, and get the basic SST modes in SO on the low frequency as well as their features and influencing factors. We will also compare the leading modes of variability against simple null hypotheses such as isotropic diffusion (red noise) and atmospheric forcings only (Slab Ocean simulation), to test the factors influence the generation and proposition of the modes (see Dommenget, 2007 and Wang et al. 2015).

The paper is organized as follows: firstly, section 2 presents the data used. Section 3 evaluates the consistency of CMIP5 simulations. The main results of this study are shown in Section 4. Here the leading modes in the Southern Ocean and their features are presented and analysis of the sources of the modes and the factors affecting the their main characteristics are presented. Finally a summary and discussion are provided in section 5.

2. Data, model simulations and methods

The observed global monthly mean SSTs are taken from the NOAA Optimum Interpolation Sea Surface Temperature (OISST) V2 from 1982 to 2004, which are based on in-situ and satellite observations (referred as “observations” below, Reynolds et al., 2002). Hadley Centre Sea Ice and SST data set (HadISST, Rayner et al., 2003) was chosen as an auxiliary.

Our analysis focuses on the long-term internal natural variability, therefore the scenario of CMIP5 "pre-industrial control" (PiControl) is used for the following study for its relatively long output without anthropogenic forcing influence. 10 CMIP5 models (Table. 1) are selected from the CMIP5 datasets (Taylor et al., 2012), as they represent all the models having at least 500 years continuous simulation and all the variable outputs needed for the analysis in this paper. We take 500 years from each model and concatenate the SST anomalies (computed for each model individually) to generate a CMIP5 super model with 5000 years of data to provide a synthesis. This kind of super model has been shown to be more similar to the observed modes than individual models (Bayr and Dommenget, 2014; Wang et al., 2015). We will further verify the super model performance in section 3.

We also use a 500 years long simulation of an atmospheric GCM coupled to a simple Slab Ocean to compare against the CMIP5 models. This model composes of the UK Meteorological Office Unified Model general circulation model with HadGEM2 atmospheric physics, a Slab Ocean model with a 50m-layer thickness and prescribed sea ice climatology. A flux correction scheme is used to force the model SST to closely follow the Hadley Centre Sea Ice and SST data set (HadISST) SST climatology (for more details see Wang et al., 2015).

All data sets (models and observations) were interpolated to a common 2.5° latitude × longitude grid and linearly detrended to remove the global warming signal and/or climate drift prior to the analysis.

The concept of the data set SST mode comparison is based on Dommenget (2007) and Bayr and Dommenget (2014), and has been applied in a similar way to the SO SST modes in Wang et al. (2015). It is briefly summarized as follows: Assume there are two data sets A and B. c_{ij} is the correlation coefficient describing the spatial similarity between $\vec{E}_i^A$, the ith EOF-pattern of A, and $\vec{E}_i^B$, the jth EOF-pattern of B. The total variance of B that can be explained by $\vec{E}_i^A$, namely projected explained variance (PEV) $pe_i^{A\to B}$, is estimated by the accumulation of all eigenvalues of B:

$$pe_i^{A\to B} = \sum_{j=1}^{N} c_{ij}^2 e_j^B \quad (1)$$

where e_j^B is the explained variance of the corresponding EOF-pattern. The overall mismatch between A and B is quantified by a normalized root-mean-square error ($RMSE_{EOF}$)

$$RMSE_{EOF}(A,B) = \sqrt{\frac{\sum_{i=1}^{N}\left(pe_i^{A\to B} - e_i^A\right)^2}{\sum_{i=1}^{N}(e_i^A)^2}} \quad (2)$$

, where A is the reference data. $RMSE_{EOF}$ ranges from 0 to 1 and estimates the inconsistency between two data sets. The larger the value is, the larger are the differences in spatial structure in variability.

Apart from the EOF projection method above, we also use the distinct EOFs (DEOFs) to estimate the patterns that describe the largest differences in explained variance between two data sets A and B (Dommenget, 2007), which are found by pairwise rotation of the EOF-modes to maximize the leading e_i^A values relative to the $pe_i^{A\to B}$ iteratively (Dommenget, 2007, Bayr and Dommenget, 2014). Each DEOF mode has two explained variance values. One is the explained variance in dataset A, $dev_i^{A\to B}(A)$, and the other the explained variance in B, $dev_i^{A\to B}(B)$. The DEOFs patterns are ordered by the difference between $dev_i^{A\to B}(A)$ and $dev_i^{A\to B}(B)$. Therefore, the first DEOF mode, $DEOF_1^{A\to B}$, would represent the pattern that explains more variance in A than in B, and this difference should be the largest among all DEOF patterns.

3. Model Evaluation

Wang et.al (2015) showed, in an evaluation of the SST modes for CMIP5 historical runs in the Southern Ocean, that the all models disagree significantly with the HadISST modes with the uncertainties in the order of 40-60% of the eigenvalues. The study also illustrated larger inconsistence of the model with each other via pairwise model comparison. However, the super model ensemble showed better agreement with the references, suggesting that it has spatial modes similar to the observed and should be more suitable for further data analysis. To verify the reliability of the models in the study here, especially the super ensemble, we will do a similar evaluation, but for the CMIP5 PiControl simulations against the OISST data.

Fig. 1 shows the leading modes of Southern Ocean monthly mean SST anomalies (south of 30°S) to get a first impression of how similar model simulations and observations are. Each EOF pattern is multiplied by the root of its own eigenvalue for consistency that the amplitude of all patterns is in the unit of Kelvin. There are clear similarities between the observed and the CMIP5 super ensemble. They both have the annular mode as the EOF-1, with the similar structure: maximum anomaly amplitude in the South Pacific and the out-of-phase zonal anomalies around 30-45°S (Fig. 1a and d). The CMIP5 super ensemble also has a similar wave train like EOF-3 as observed (Fig. 1c and f). However, the EOF-2 in CMIP5 is more like a wave-3 pattern along 60°S with two weak troughs (Fig. 1e) while differently the observed EOF-2 composes of 4 waves (Fig. 1b).

The Slab Ocean results (Fig. 1g-i) illustrate more differences with much larger eigenvalues compared to observations and CMIP5 data. Its EOF-1 (Fig. 1g) shows similar wave-3 structure as CMIP5 EOF-2, but the two weak troughs get much stronger in the Slab Ocean simulation south to Africa/Australia. Another wave-3 pattern also exists within the Slab Ocean EOF-2 (Fig. 1h) and its anomaly centres in the Pacific are in the same location as the annular mode (EOF-1) in CMIP5 and the observed. Last but not least, Slab Ocean has a similar wave-like EOF-3 as its counterparts but with lower latitude centres.

To quantify the differences among data sets, Fig. 2 presents the $RMSE_{EOF}$ with OISST as reference on the x-axis and all models as references on the y-axis. The values on the y-axis are the mean $RMSE_{EOF}$ of all pairwise comparison with all individual models as references.

OISST and HadISST for the same period (1982-2014) agree well with each other, since the two observational data sets contain the same observations. However, the HadISST data for the much longer period (1901-2014) disagrees with the OISST data substantially. This is most likely due to the sparse observations prior to the 1980s. The relative errors of most models are ranging from 20% to 45% of the eigenvalues, which are substantial and similar as the difference between Slab Ocean and the observed (29%). The CMIP5 super model performs better (28%) than most models

and has by construction much longer statistics than any individual model, which suggests that the super model is the best data set for the following analysis.

For the model pairwise comparison, most models are in the range of 20% to 50%, while the observed has larger bias of 50%~65%. This indicates that models have strong differences and disagreements in the spatial structures between each other. Again the super model is better than most individual models with an error of 26%, implying the model ensemble should be a good substitution of an individual model.

The slab ocean shows substantial difference relative to the models (60% error), which suggest that the dynamics of the CMIP5 models are significantly different than in the slab ocean model. Additionally, we introduce two categories of isotropic diffusions representing homogeneous spatial red noise processes (refer as $H0_{uniform}$) and spatial red noise with known standard spatial deviation pattern (refer as $H0_{STDV}$) (see Dommenget 2007 and Wang et al. 2015 for details). Both these simple stochastic models are farther away from the observations than any individual model, suggesting that the SST modes in the Southern Ocean are indeed related to more complex dynamics than assumed in the simple null hypotheses.

4. Leading Modes in the Southern Ocean

In this section we present the main results of this analysis, the leading modes in the Southern Ocean and possible factors for their generation and propagation. As a start Fig. 3 firstly depicts the standard deviation (STDV) of annual mean SST anomalies from OISST, CMIP5 ensemble mean and Slab Ocean simulation. The OISST has maximum variation south to Africa, around New Zealand and in the middle of South Pacific. The CMIP5 runs simulate most of the observed structures of the STDV distribution successfully, but underestimate the variability for the most active areas and tend to have stronger fluctuation within the sea ice region around Antarctic. The spatial structure of the STDV in the slab ocean simulation is too smooth, but with similar overall amplitudes. The regions around the sea ice boarder have by construction no SST variability, as the model has prescribed sea ice climatologies.

Fig. 4 shows the fraction that the long-term SST variability (>10 years) contributes to the total annual mean variation based on the CMIP5 super model ensemble. Note that

most of the high latitude oceans are dominated (>60%) by low-frequency variations, while in the tropics it contributes less than 30%. In the Southern Ocean, the long-term signal is stronger in the higher latitudes and in the Indian Ocean it appears to reach from the south-west to north-east, while one branch reach the south of Australia and the Tasmanian Sea.

The leading modes of SST variability in the CMIP5 super model on different time scales including monthly mean, annual mean and 5 years running mean are shown in Fig. 5 based on EOF-analysis. A few characteristics can be noted here:

- The three leading modes on the monthly mean time scale all together explain only about 26%, which indicates a fairly large number of spatial degrees of freedom ($N_{spatial}$ = 27, see Bretherton et al., 1999 for the definition). This $N_{spatial}$ here is larger than in most other ocean basins (Wang et al. 2015) and thus indicates the complexity of the SO SST variability. On the longer time scales the relative importance of the leading modes increases, with more than 40% explained by the three leading modes. This indicates that on the longer time scales the leading modes of SST variability become larger in spatial scale and the SST variability overall becomes less complex ($N_{spatial}$ = 13 for 5yrs running mean).
- The monthly mean EOF-1 corresponds to EOF-1 on annual mean and EOF-2 on 5 years running mean. All three of them illustrate the annular structure with the maximum anomalies in the Pacific, corresponding to the region with large SST STDV in Fig. 3b. The relative importance (eigenvalue) of this pattern appears to be strongest in the annual mean SST variability. It becomes less important on the longer than 5yrs time scales.
- The EOF-2 of monthly mean, as described above (Fig. 1), is a wave-train like pattern with three clear crests, which is much more pronounced in the slab ocean simulation (Fig.1g). When it comes to annual mean time scales (EOF-2 in Fig. 5e), the troughs become much less conspicuous and the crest in the Southern Atlantic intensified while the other two crests get much weaker. The corresponding pattern on the even longer time scale (EOF-1 in Fig. 5g) has the no more signature of the three-wave structure and it leaves a monopole pattern. Thus it appears that the atmospheric three wave pattern forcing is very clear in

the slab ocean simulation and then transforms into a basin wide monopole pattern in the dynamical ocean simulations of the CMIP5 super model ensemble on longer decadal time scales. The eigenvalue of this mode is increasing as the time scale gets longer from 7% to 21% and it becomes the leading pattern on the 5yrs running mean analysis, implying that this pattern is more dominant on decadal scale.

- The EOF-3 pattern doesn't seem to change much over the varying time scales. The time series of EOF-3 has strong correlation with its counterpart on the different time scales ($r > 0.7$), implying all the EOF-3s belong to basically the same mode and its temporal variation is well kept, however, its spatial pattern gradually transform from wave-train pattern to a dipole structure in the Pacific on the annual mean scale with anomalies moved to the higher latitudes. The dipole pattern further fades as the pole in the west Pacific weakens on the longer time scale.

In the following analysis we will focus on the annual mean modes, as we are mostly interested in long time SST variability. The power spectra of the leading annual mean EOF-modes are illustrated in Fig. 6. For comparison with the slab ocean simulation we project the CMIP5 annual mean EOF-modes onto the slab ocean data to estimate the time series that these patterns would have in the slab ocean simulation. The power spectra of these time series are shown in for Fig. 6 comparison. Thus we here consider the slab ocean as being a simple red noise test as discussed in the stochastic climate model by Hasselmann (1976). The theoretical red noise power spectrum is fitted to the slab ocean power spectrum in Fig. 6. A number of interesting characteristics can be noted in these power spectra:

- All three CMIP5 super ensemble modes have more variability on the longer time scales than the slab ocean simulations. Thus it indicates that in all three modes ocean dynamics may be key in producing the long time SST variability.
- The EOF-1 mode has a very similar shape of the power spectrum in both the CMIP5 super model and the slab ocean, but the CMIP5 super model power spectrum is shift higher up, indicating it has more variance on all time scales.
- The EOF-2 mode has a very interesting time scale behavior that deviates from a red noise power spectrum quite substantially. It appears to be similar in

amplitude and time scale behavior to the slab ocean for interannual until about decadal time scales. But on multi-decadal time scales the CMIP5 super model SST variability starts to increase again by about an order of magnitude for the centennial time scales. Thus the EOF-2 mode has a two-step power spectrum, with an interannual to decadal level of variance and a second higher up level of variance on the multi-decadal to centennial time scales.

- The EOF-3 mode has a similar indication of increased variance on the longer time scales compared to the slab ocean, but it is not as strong and it seem to have a more pronounce time scale (peak) at around 50yrs periods.

To further explore the origin of the spatial structures of the leading modes we take a closer look at the leading modes in the Slab Ocean simulation and in the simple spatial red noise patterns H0-STDV (see Fig. 7). The leading modes of the slab ocean simulation are dominated be the wave number three wave-train shapes that are forced by the atmospheric wave trains. The patterns also show no substantial changes from monthly mean (Fig. 1g-i) to annual mean time scales, suggesting that the pattern are present on all time scales. The simple spatial red noise H0-STDV EOF-modes are a hierarchy of multi-poles (Fig. 7d-f), starting with a monopole (largest scale), followed by dipoles with increasing complexity (see Dommenget 2007 for a more detailed discussion). These multi-pole modes are centered on the regions of large SST STDV (see Fig. 3b).

The modes of the Slab Ocean simulation and H0-STDV stochastic null hypothesis are clearly different to CMIP5 super model ones. The DEOF modes shown in Fig. 8 further quantify these differences. The DEOF modes represent the modes that in the comparison between the CMIP5 super model and the Slab Ocean simulation or H0-STDV stochastic null hypothesis are most dominant in the CMIP5 super model (see methods section for details on the DEOF-modes).

Most of the leading DEOF modes duplicate the leading CMIP5 modes in Fig. 5d-f, suggesting that the Slab Ocean and red noise H0-STDV process do not produce these leading modes with enough variance. This is also consistent with the comparison of the power spectra in Fig. 6, where we found that the slab ocean power spectrum of EOF-1 was much weaker than in the CMIP5 super model. One exception is the

DEOF-3 for the Slab Ocean (Fig. 8c). This DEOF mode is not similar to the CMIP5 EOF-3 and is more concentrated along the Antarctica.

In summary of this first part of this analysis we can say that we have three leading modes of SST variability on the interannual and long time scales, which all three are fairly different in either their patterns or in there amount of variance from what you would expect from a simple red noise integration of atmospheric forcings. Thus all three modes are likely to involve ocean dynamics to create the pattern or at least the amount of variance. In the following we want to discuss the characteristics of these modes a bit more in detail. However, it will be beyond the scope of this work to fully explain the physical mechanisms of all three leading modes.

4.1 Mode 1: The Annular Mode

The first annual mean mode is descripted as the annular mode, which is also the leading mode within monthly mean analysis and has a similar structure as the SAM. Besides, the strong anomalies of the mode in the Pacific suggest it is related to ENSO as well. The SAM index (difference in the normalized monthly zonal-mean sea level pressure between 40°S and 65°S, Gong and Wang, 1999) leads the time evolution of this mode by about one month and the Niño 3.4 SST index (average SST anomaly in the region of 5°N to 5°S, 170°W to 120°W) leads by several months (Fig. 9). Thus we have two important atmospheric teleconnections that drive this mode. The global monthly mean SSTA correlation with Niño 3.4 and SAM indices are also shown in Fig. 10. Both the correlation distributions in the Southern Ocean show similar spatial structure as this annular mode itself. However, obviously the correlation focuses within the South Pacific domain in the Southern Ocean when correlated with ENSO, while the SAM correlation is extended to the entire ocean.

To further discuss these two effects separately, we divide the Southern Ocean into two regions, namely the Pacific part (150°E to 60°W) and the Atlantic-Indian part (rest of the SO), and compute the respective EOF modes for the CMIP5 super model (see Fig. 11). The corresponding spatial patterns (EOF-1 for the South Pacific sector and EOF-2 for the Indian-Atlantic domain) are almost identical to the Southern Ocean pattern (EOF-1 in Fig. 5d). The correlation between the Southern Ocean pattern and

Pacific one is 0.9, and it is 0.7 between entire ocean time series and Atlantic-Indian Ocean counterpart; but it is only 0.5 for the two separated region comparison.

We construct a simple linear model for the variability of these EOF time series based on ENSO and SAM impacts:

$$H_n = \alpha H_{n-1} + \beta Nino34_n + \gamma SAM_n + f \quad (3)$$

, where H_n is the value of the time series in the n^{th} year in the CMIP5 models, α is the memory of the ocean, β and γ are the linear forcing coefficients for normalized Niño 3.4 and SAM indices, respectively. f is the residual. Thus, larger absolute value of β (γ) represents stronger impact from ENSO (SAM) on the temporal variability. The results of a least squared fit to the CMIP5 super model data are listed in Table. 2. As expected, ENSO shows strong influence in the Pacific and limited impact for the rest domain. SAM has almost the same influence on both individual regions. For the entire basin, the impacts of these two phenomena are comparable to each other and also to the ocean memory. The reconstructed time series H_n has strong correlation (r = 0.8) with the Southern Ocean EOF-1 time series and it basically reproduces the spatial structure of EOF-1 (see Fig. 12). Similar results are also found within the observation (β = - 0.54 , γ =0.31 for OISST annual mean EOF-1 in the SO). Thus, this annular mode is driven by ENSO and SAM.

In this context it is interesting to note that the slab ocean simulation has much less variance in this mode (see Figs.6a and 8a), although it is forced by the SAM. ENSO forcing does not exist in the slab ocean simulation, since ENSO is not simulated in the slab ocean simulation, but it is unlikely that this is the main reason why the mode is much weaker in the slab ocean simulation. Both SAM and ENSO mostly affects the Southern Ocean via the variation of zonal winds and thus by wind induced mixing (e.g. Sallée et al., 2010; Screen et al., 2010). But wind mixing does not exist in the slab ocean simulation. The relation to wind forcing is also highlight by the fact that the main node of EOF-1 is around the 60°S to 40°S latitudes band, which is also where the SAM pattern has its maximum sea level pressure gradients and thus the strongest wind stress forcings.

4.2 Mode 2: Basin wide monopole mode

We name the annual mean EOF-2 the basin wide monopole mode as its anomalies expand with the same sign over the entire SO domain on longer scales. This kind of spatial structure is more apparent on even longer time scale (10 years running mean to 50 years running mean) as shown in Fig. 13. The eigenvalues are increasing with longer time scales indicating the increasing importance of this mode for longer time scales. Thus, this pattern, as the leading pattern on interannual scale already, becomes more dominant on decadal and multi-decadal scales, which is consistent with the internal centennial variability (Martin et al., 2013; Latif et al., 2013).

This pattern, as mentioned in the previous sections, originates from a wave number three wave-train prototype pattern in the slab ocean EOF-1 without ocean dynamics. Thus it is forced from the atmospheric heat flux forcing at least partially. Fig. 14 shows the correlation of the time series of EOF-2 with the geopotential height at 500hPa. The three wave crests can be recognized in the atmosphere and the nodes are well collocated with the nodes of the SST pattern (Fig. 5b).

To further analyse the relation of the SST to the atmosphere and the subsurface ocean we create an SST index based on the three crests boxes (0-30°W, 40°S-60°S for Box-1; 60°-90°E, 40°S-60°S for Box-2 and 160°E-170°W, 40°S-60°S for Box-3) and make the boxed averaged value as a SST proxy index for this mode. The SST index has a correlation of 0.9 with the annual mean EOF-2 and thus illustrates that the EOF-2 mode is indeed mostly the variability in these three regions combined. The 500hPa geopotential height index of the same boxes leads the SSTA index by about one month (see Fig. 15a). Thus, the atmospheric internal wave-3 structure is a forcing of this SST pattern.

In the CMIP5 super model it appears that the pattern transforms from the wave-3 structure on the shorter monthly mean time scales to the basin wide monopole mode pattern on the decadal and longer time scales. In the Slab Ocean simulation this development does not happen and the SST variability keeps the wave-train structure on the longer time scales (Fig. 1g and Fig. 7a). This is also reflected in weaker power spectrum for this mode in the slab ocean simulation (Fig. 6b). This suggests that the ocean dynamics may be the essential factor responsible for the mode transformation and power spectrum increase on multi-decadal and longer time scales.

The vertical structure of this mode in the upper ocean may give some indication of its nature. For this we take a look at the lag-lead correlation between the SST mode index and the ocean temperature at different depths, and we look at the pattern of the in phase (zero lag) correlation between the SST mode index and the ocean temperature at different depths (see Fig. 15).

The SST evolution appears to lead the subsurface temperature evolution on all layers and signal generally gets weaker the deeper we go (Fig. 15a-b). However, it is interesting to note that the correlation in 500m depths is larger than in the upper ocean layers when the SST is leading by more than two years. It is also interesting to note that the patterns transforms slightly from a monopole at the surface to an annular dipole structure at 500m depth (Fig. 15c).

4.3 Mode 3: Dipole Mode in the South Pacific

The EOF-3 is a dipole in the South Pacific on annual mean scale (shown in Fig. 5f). It also starts from a zonal wave pattern shown in Fig. 5c on shorter time scale, but the wave pattern is out of phase with that of EOF-2. The anomalies in the Atlantic and Indian Ocean get weaken on longer time scales, while the pattern gets transformed gradually and more focuses within Pacific on annual mean time scale. The western pole in the South Pacific also loses its strength on longer time scale, making this pattern concentrate around Antarctica (Fig. 5i). To illustrate that this pattern is indeed mostly in the Pacific sector of the SO we again look at the EOF-modes of the Pacific region (EOF-2 as shown in Fig. 16). This EOF-2 mode of the South Pacific has a correlation of 0.95 with the annual mean time series of Southern Ocean EOF-3.

For the further analysis we simplify the SST mode by a dipole index (hereafter as $\text{Index}_{\text{A-B}}$) over the two main centres (Box-A: 45°S-70°S, 120°W-80°W and Box-B: 45°S-60°S, 180°-140°W). This index matches the EOF-3 time series fairly well (correlation = 0.89 for annual mean analysis). Fig. 17 depicts the correlation between monthly SSTA $\text{Index}_{\text{A-B}}$ and 500hPa geopotential height anomaly. Again it demonstrates another wave-3 structure, but the maximum anomalies are mostly restricted within the South Pacific. The crests are around New Zealand, south to South America and South to Africa, and the troughs are mostly in the middle of the oceans.

As for Mode-2 we again look at the lag-lead correlation between the SST $\text{Index}_{\text{A-B}}$ and the ocean temperature at different depths and we look at the pattern of the in phase (zero lag) correlation between the SST $\text{Index}_{\text{A-B}}$ and the ocean temperature at different depths (see Fig. 18). As expected the geopotential height variation leads the SST variability for one month, demonstrating that the atmosphere also drives this dipole mode. The SST also leads the deeper water temperature anomalies as well, but the influence decreases more rapidly with lead/lag time (Fig. 18b), which is consistent with the power spectrum having less multi-decadal variance than the Mode-2. However, the lag-lead relationship to the 500m depths temperature appears to somewhat different than in Mode-2. Here the 500m depths temperature has strong correlation with the SST $\text{Index}_{\text{A-B}}$ when the 500m depths temperature is leading, which may suggest a subsurface ocean influence on the SST $\text{Index}_{\text{A-B}}$ on the longer time scales. The SST pattern also has some minor changes with depth (Fig. 18c). The western pole in the Pacific gets weaker, which might explain why the western pole also becomes unclear on the longer scale on the surface.

5. Summary and Discussion

In the study presented here we discussed the leading modes of SST variability in the Southern Ocean on long, decadal time scales in CMIP5 preindustrial scenario simulations. We compared the CMIP5 simulations with observations, simple stochastic null hypothesis for the spatial structure of SST variability and against a simulation with a slab ocean that does not simulate any ocean dynamics. This study illustrated a number of interesting modes dominating the Southern Ocean. We list the main findings below:

- First it is important to note that current state of the art CMIP5 simulations have large inconsistencies against the observation and with each other. Our understanding of the leading modes of SST variability is therefore still limited and is likely to have substantial biases. However, using the CMIP5 super model ensemble of all available models does have some advantage in smoothing out model biases and is therefore a good basis for the analysis of the SO SST modes.

- The SST modes of the SO are the most complex of all ocean basins (Wang et al. 2015). They have the largest effective spatial degrees of freedom of all ocean basins and the leading three EOFs only contribute 26% (monthly scale) to 42% (5 years running mean) of the total variance. It implies that higher order modes contribute to the SST variability significantly and are potentially also relevant for understanding the leading modes.
- All three leading modes found in the CMIP5 super model have distinct patterns and time scale behavior that can not be explained by simple stochastic null hypothesis, like spatial red noise (isotropic diffusion), nor by a slab ocean dynamics. Thus all three leading modes are ocean-atmospheric coupled modes and are likely to be substantially influenced or driven by ocean dynamical processes.
- The first leading mode is described as an annular mode. It is forced by two main drivers: ENSO and SAM. ENSO mainly influences the Pacific part of the mode while SAM impacts the entire basin of the Southern Ocean. The impact of these drivers is much stronger in the CMIP5 simulations than in the slab ocean simulation, suggesting that it is mostly the wind stress forcing that drives the SST variability of this mode. This is also consistent with the position of the main amplitudes of this mode being at the same locations as the maximum wind variability being associated with the SAM index.
- The second most dominant mode is a basin wide monopole pattern. It transforms for the atmospherically forced three-wave pattern on shorter time scales to an all basin wide mode on multi-decadal time scales. Such a transformation is not observed in the slab ocean simulation suggesting it involves ocean dynamics. A potential candidate for such a transformation could be lateral advection by ocean transport and stochastic resonance with atmospheric forcing. However, it was beyond the scope of this study to understand the details of these processes. This mode further has a very distinct time scale behavior with a significant increase of variance from the decadal time scales to even longer centennial time scales that is very clearly distinct from the behavior of the slab ocean simulation. Thus this mode has a lot of power on very long time scales that are strongly related to ocean dynamical processes.

- The third leading mode is a dipole structure in the South Pacific. It also originates from the atmospheric forcing of three-wave pattern, but unlike the monopole pattern its variance is not increasing as much on multi-decadal and longer time scales. However, this pattern appears to have a peak in the power spectrum, suggesting a preferred time scale of oscillation. This mode also has some weak indications of the subsurface ocean temperature leading the evolution of the SST variability on the longer (~10yrs) time scales. This indicates that this mode may be influenced by deeper ocean variability on the longer time scales. There are a few studies about dipole structures in the South Pacific, e.g. Huang and Shukla (2006), Morioka et al. (2013) and Guan et al. (2014). However, their results actually are parts of the annular mode in north-south direction or monopole mode in the Pacific, which is not the same as this pattern.
- Another question is the possible interactions among these modes. As discussed above, the Annular Mode is partly driven by SAM. On the other hand, the strengthened westerlies caused by positive SAM above the Southern Ocean may alter the ocean circulation pattern and introduce more mixing locally (e.g. Meredith and Hogg, 2006; Boning et al, 2008). These changes might lead to the evolution of the monopole mode and dipole mode in the South Pacific, though the correlation between SAM and these two modes within CMIP5 super ensemble is unclear. Besides, the monopole mode and dipole mode, as they have similar mechanisms and wave train prototypes, might have the out-of-phase relationship. However, the lead-lag correlations are obscure in CMIP5 dataset and the interactions require further studies.

As monopole mode and dipole mode in South Pacific are mainly influenced by ocean dynamics, it is essential to understand the different effects of within the ocean. The related phenomenon includes but are not limited to a different zonal wave-3 pattern (Loon and Jenne, 1972; Raphael, 2004), the ACC and its related Antarctic Circumpolar Wave (ACW, White and Peterson, 1996; White et al., 1998), ocean diffusion mixing and deep ocean circulation. These factors above have close relationship with each other but are also relatively independent with their own specific period. For instance, the ACC has the main period of 4-5 years, the ACW could circling the globe each 8-9 years, while the diffusion and thermohaline

circulation own a multi-decadal or centennial variation. The interactions between them should be the critical step for a deeper understanding of the modes.

Another important factor is sea ice, which also influences atmospheric circulations substantially and is capable of introducing long-term variability. The ice-sea interaction affects the SST variability and further influences the mode spatial structure and temporal variation. As our slab ocean model does not create sea ice variability, the role of sea ice is not fully discussed above. The sea ice impact requires more detailed numerical model experiments.

Acknowledgements

We like to thank Dr Claudia Frauen for fruitful discussions and comments. The ARC Centre of Excellence in Climate System Science (CE110001028) supported this study. The Slab Ocean model simulations were computed on the National Computational Infrastructure in Canberra.

References

Bayr T, Dommenget D (2014) Comparing the spatial structure of variability in two datasets against each other on the basis of EOF modes. Clim Dyn 42: 1631-1648.

Böning CW, Dispert A, Visbeck M, Rintoul SR, Schwarzkopf FU (2008) The response of the Antarctic Circumpolar Current to recent climate change. Nature Geosci 1: 864-869

Boer GJ, Fourest S, Yu B (2001) The signature of the annular modes in the moisture budget. J Clim 14:3655–3665

Bretherton CS, Widmann M, Dymnikov VP, Wallace JM, Bladé I (1999) The effective number of spatial degrees of freedom of a time-varying field. J Clim 12: 1990-2009

Cai W, Watterson IG (2002) Modes of interannual variability of the southern hemisphere circulation simulated by the CSIRO climate model. J Clim 15:1159–1174

Cavalieri DJ, Parkinson CL (2008) Antarctic sea ice variability and trends, 1979–2006, J Geophys Res 113: C07004, doi: 10.1029/2007JC004564

Comiso JC, Nishio F (2008). Trends in the sea ice cover using enhanced and compatible AMSR-E, SSM/I, and SMMR data. J Geophys Res 113: C02S07, doi: 10.1029/2007JC004257

Cook ER, Buckley BM, D'Arrigo RD, Peterson MJ (2000) Warm-season temperatures since 1600 BC reconstructed from Tasmanian tree rings and their relationship to large-scale sea surface temperature anomalies. Clim Dyn 16 (2–3): 79–91

Dommenget D (2007) Evaluating EOF modes against a stochastic null hypothesis. Clim Dyn 28(5): 517-531

Fyfe JC (2003) Separating extratropical zonal wind variability and mean change. J Clim 16: 863-874

551 Gong DY, Wang SW (1999) Definition of Antarctic Oscillation index. Geophys Res
552 Lett 26: 459–462.

553 Guan Y, Zhu J, Huang B, Hu Z-Z, Kinter III JL (2014) South Pacific Ocean Dipole:
554 A predictable mode on multiseasonal time scales. J Clim 27: 1648–1658

555 Hasselmann K (1976) Stochastic climate models Part I. Theory. Tellus 28(6): 473-485.

556 Hogg AM, Blundell JR (2006) Interdecadal Variability of the Southern Ocean. J Phys
557 Oceanogr 36: 1626–1645.

558 Huang B, Shukla J (2006) Interannual SST variability in the southern subtropical and
559 extra-tropical ocean. Tech Rep 223: 20 pp. Cent for Ocean Land Atmos Stud,
560 Calverton, Md

561 Jones PD, Salinger MJ, Mullan AB (1999) Extratropical circulation indices in the
562 Southern Hemisphere based on station data. Int J Climatol 19: 1301-1317

563 Jones JM, Fogt RL, Widmann M, Marshall GJ, Jones PD, Visbeck M (2009)
564 Historical SAM Variability. Part I: Century length seasonal reconstructions. J Clim 22:
565 5319-5345

566 Karoly, DJ (1989) Southern hemisphere circulation features associated with El Niño-
567 Southern Oscillation events. J Clim 2: 1239-1252

568 Karoly DJ (1990) The role of transient eddies in low-frequency zonal variations of the
569 Southern Hemisphere circulation. Tellus 42A: 41–50

570 Kidson JW (1998) Indices of the Southern Hemisphere zonal wind. J Clim 1: 183-194

571 Kidson JW, Renwick JA (2002) The Southern Hemisphere evolution of ENSO during
572 1981-1999. J Clim 15: 847-863

573 Latif M, Martin T, Park W (2013) Southern Ocean sector centennial climate
574 variability and recent decadal trends. J Clim 26: 7767–7782.

575 Mantua NJ, Hare SR (2002) The Pacific Decadal Oscillation. J Oceanogr 58: 35 – 44

576 Martin T, Park W, Latif M (2013) Multi- centennial variability controlled by Southern
577 Ocean convection in the Kiel Climate Model, Clim Dyn, 40(7): 2005-2022

578 Meredith MP, Hogg AM (2006) Circumpolar response of Southern Ocean eddy
579 activity to a change in the Southern Annular Mode. Geophys Res Lett 33: L16608,
580 doi: 10.1029/2006GL026499

581 Mo KC, Higgins RW (1998) Tropical influences on California precipitation. J Clim
582 11: 412–430

583 Morioka Y, Ratnam JV, Sasaki W, Masumoto Y (2013) Generation mechanism of the
584 South Pacific Subtropical Dipole. J Clim 26: 6033–6045.

585 North GR, Bell TL, Cahalan RF, Moeng FJ (1982) Sampling errors in the estimation
586 of empirical orthogonal functions. Mon Wea Rev 110: 699-706

587 O'Kane TJ, Matear RJ, Chamberlain MA, Risbey JS, Sloyan BM, Horenko I (2013)
588 Decadal variability in an OGCM Southern Ocean: Intrinsic modes, forced modes and
589 metastable states. Ocean Model 69: 1-21.

590 Raphael, M.N., 2004: A zonal wave 3 index for the Southern Hemisphere. Geophys.
591 Res. Lett., 31, L23212, doi: 10.1029/2004GL020365

592 Rayner NA, Parker DE, Horton EB, Folland CK, Alexander LV, Rowell DP, Kent EC,
593 Kaplan A (2003) Global analyses of sea surface temperature, sea ice, and night
594 marine air temperature since the late nineteenth century. J Geophys Res 108:
595 D144407, doi:10.1029/2002JD002670

596 Renwick JA (2002) Southern Hemisphere circulation and relations with sea ice and
597 sea surface temperature. J Clim 15: 3058-3068

598 Reynolds RW., Rayner NA, Smith TM, Stokes DC, Wang W (2002) An improved in
599 situ and satellite SST analysis for climate. J Clim 15: 1609-1625.

600 Sabine CL, Feely RA, Gruber N, Key N, Lee K, Bullister JL, Wanninkhof R, Wong
601 CS, Wallace DWR, Tilbrook B, Millero FJ, Peng T-H, Kozyr A, Ono T, Rios, AF
602 (2004) The oceanic sink for anthropogenic CO_2. Science 305(5682): 367-371

603 Sallée JB, Speer KG, Rintoul SR (2010) Zonnally asymmetric response of the
604 Southern Ocean mixed-layer depth to the Southern Annular Mode. Nature Geosci 3:
605 273-279

606 Screen JA, Gillett NP, Karpechko AY, Stevens DP (2010) Mixed layer temperature
607 response to the Southern Annular Mode: Mechanisms and model representation. J.
608 Clim 23: 664–678.

609 Séférian R, Iudicone D, Bopp L, Roy T, Madec G (2012) Water mass analysis of
610 effect of climate change on air–sea CO_2 fluxes: the Southern Ocean. J Clim 25: 3894–
611 3908

612 Taylor KE, Stouffer RJ, Meehl GA (2012) An overview of CMIP5 and the
613 experiment design. Bull Amer Meteor Soc 93: 485-498

614 Thompson DWJ, Wallace JM (2000) Annular modes in the extratropical circulation.
615 Part I: Month-to-month variability. J Clim 13: 1000–1016

616 Turner J (2004) Review, The El Niño Southern Oscillation and Antarctica. Int J
617 Climatol 24: 1-31

618 Villalba R, Boninsegna JA, Veblen TT, Schmelter A, Rubulis S (1997) Recent trends
619 in tree ring records from high elevation sites in the Andes of northern Patagonia. Clim
620 Chang 36: 425-454

621 van Loon, H., and R. L. Jenne (1972), The zonal harmonic standing waves in the
622 Southern Hemisphere, J Geophys Res 77, 992–1003, doi: 10.1029/JC077i006p00992

623 Wang G, Dommenget D, Frauen C (2015) An evaluation of the CMIP3 and CMIP5
624 simulations in their skill of simulating the spatial structure of SST variability. Clim
625 Dyn 44: 95-114.

626 White WB, Peterson RG (1996) An Antarctic circumpolar wave in surface pressure,
627 wind, temperature, and sea-ice extent. Nature 380: 699-702

White WB, Chen SC, Peterson RG (1998) The Antarctic Circumpolar Wave: A beta effect in ocean-atmosphere coupling over the Southern Ocean. J Phys Oceanogr 28: 2345–2361

Yuan X, Li C (2008) Climate modes in southern high latitudes and their impacts on Antarctic sea ice. J Geophys Res-Oceans 113: C06S91.

Yuan X, Yonekura E (2011). Decadal variability in the Southern Hemisphere. J Geophys Res 116: D19115, doi:10.1029/2006JC004067

Table Captions

Table. 1 List of CMIP5 models

Table. 2 Parameters of linear regression model for annual mean EOF-1 time series discussed in the text.

Figure Captions

Fig. 1 First three leading EOF patterns of detrended monthly SSTA in the Southern Ocean for (a-c): Observation (OISST); (d-f): CMIP5 super model; (g-i): slab ocean experiment. The values in the headings of each panel are the explained variances of each EOF-mode.

Fig. 2 $RMSE_{EOF}$ values distribution relative to the observations (x axis) and mean $RMSE_{EOF}$ values of pairwise comparisons to all CMIP5 model simulations (y axis) for monthly SSTA EOF-analysis in the Southern Ocean. The sampling uncertainty is based on North et al. (1982) and Wang et al (2015).

Fig. 3 Standard deviation fields of annual mean SSTA for (a): OISST; (b): CMIP5 super model; (c): Slab Ocean experiment result.

Fig. 4 The relative contribution of Long-term (> 10 years) variability to the total of annual mean variations based on the CMIP5 super model.

Fig. 5 First three leading EOF patterns of CMIP super model SSTA in the Southern Ocean for (a-c): monthly mean; (d-f): annual mean; (g-i): 5 years running mean. The values in the headings of each panel are the explained variances of each EOF-mode.

Fig. 6 Spectrum of the time series of the three leading EOF-modes of the CMIP super model annual mean SSTA (as in Fig. 5d-f). The power spectrum of the time series resulting from the projection of these patterns onto the slab ocean simulation SST variability are shown for comparison. The black line is a red noise fit to the slab ocean time series and the red lines mark the 95% confidence interval relative to the red noise fit of the slab ocean simulation.

Fig. 7 (a-c): First three leading EOF patterns of detrended annual mean SSTA in the Southern Ocean for (a-c): slab ocean; (d-f): H0-STDV null hypothesis. The values in the headings of each panel are the explained variances of each EOF-mode.

Fig. 8 (a-c): Leading DEOF patterns of annual mean SSTA CMIP5 projection to Slab Ocean; (d-f): Leading DEOF patterns of annual mean SSTA CMIP5 projection to H0-STDV. The headings show the explained variances of the DEOF-modes in the CMIP5

super model (first value) and the slab ocean simulation or H0-stdv null hypothesis (second value), respectively.

Fig. 9 Lead-lag correlation between Niño3.4/SAM and monthly mean PC-1 time series of CMIP super ensemble. Note that the correlation with Niño3.4 is multiplied by minus one to be positive.

Fig. 10 (a): Monthly SSTA correlation with Niño 3.4 in CMIP5 super model; (b): same as (a) but for the correlation between SSTA and SAM index.

Fig. 11 (a): CMIP5 super model EOF-1 of annual mean SST in South Pacific; (b): EOF-2 of annual mean SST in South Atlantic and Indian Ocean. The values in the headings of each panel are the explained variances of each EOF-mode.

Fig. 12 Correlation between a reconstructed SSTA PC-1 time series and SSTA of the CMIP5 super model on annual time scale. See text for details on the reconstruction model.

Fig. 13 EOF-1 of SSTA in Southern Ocean of the CMIP5 super ensemble for (a): 10 years running mean; (b) 20 years running mean; (c) 50 years running mean. The values in the headings of each panel are the explained variances of each EOF-mode.

Fig. 14 Correlation between SSTA PC-2 time series and 500hPa geopotential height anomaly of the CMIP5 super model on monthly time scale.

Fig. 15 Lead-lag correlation for box-averaged indices for the monopole mode between SSTA and 500hPa geopotential height/subsurface ocean temperature anomalies. (a): Lead-lag correlation on monthly time scale; (b): same as (a) but for annual time scale; (c): Correlation between SSTA PC-2 time series and subsurface ocean temperature of the CMIP5 super model on annual time scale.

Fig. 16 EOF-2 of CMIP5 super model SST in the South Pacific for annual mean analysis. The value in the heading is the explained variance of this EOF-mode.

Fig. 17 Correlation between Box [A-B] time series and 500hPa geopotential height anomaly of the CMIP5 super model on monthly time scale.

694 **Fig. 18** Lead-lag correlation for $\text{Indices}_{\text{A-B}}$ between SSTA and 500hPa geopotential
695 height/subsurface ocean temperature anomalies. (a): Lead-lag correlation on monthly
696 time scale; (b): same as (a) but for annual time scale; (c): Correlation between SSTA
697 PC-2 time series and subsurface ocean temperature of the CMIP5 super model on
698 annual time scale.

Figure

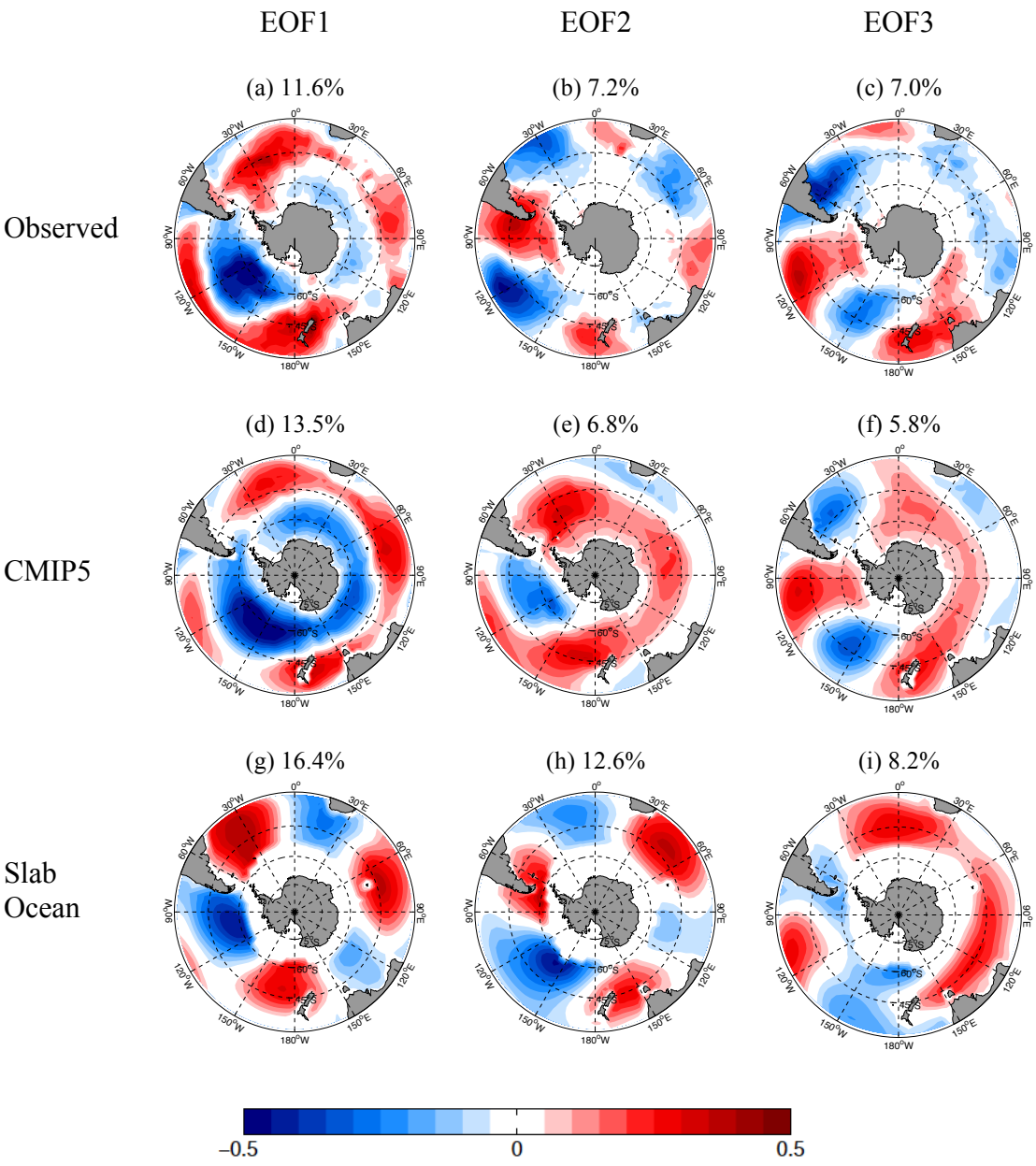

Fig. 1 First three leading EOF patterns of detrended monthly SSTA in the Southern Ocean for (a-c): Observation (OISST); (d-f): CMIP5 super model; (g-i): slab ocean experiment. The values in the headings of each panel are the explained variances of each EOF-mode.

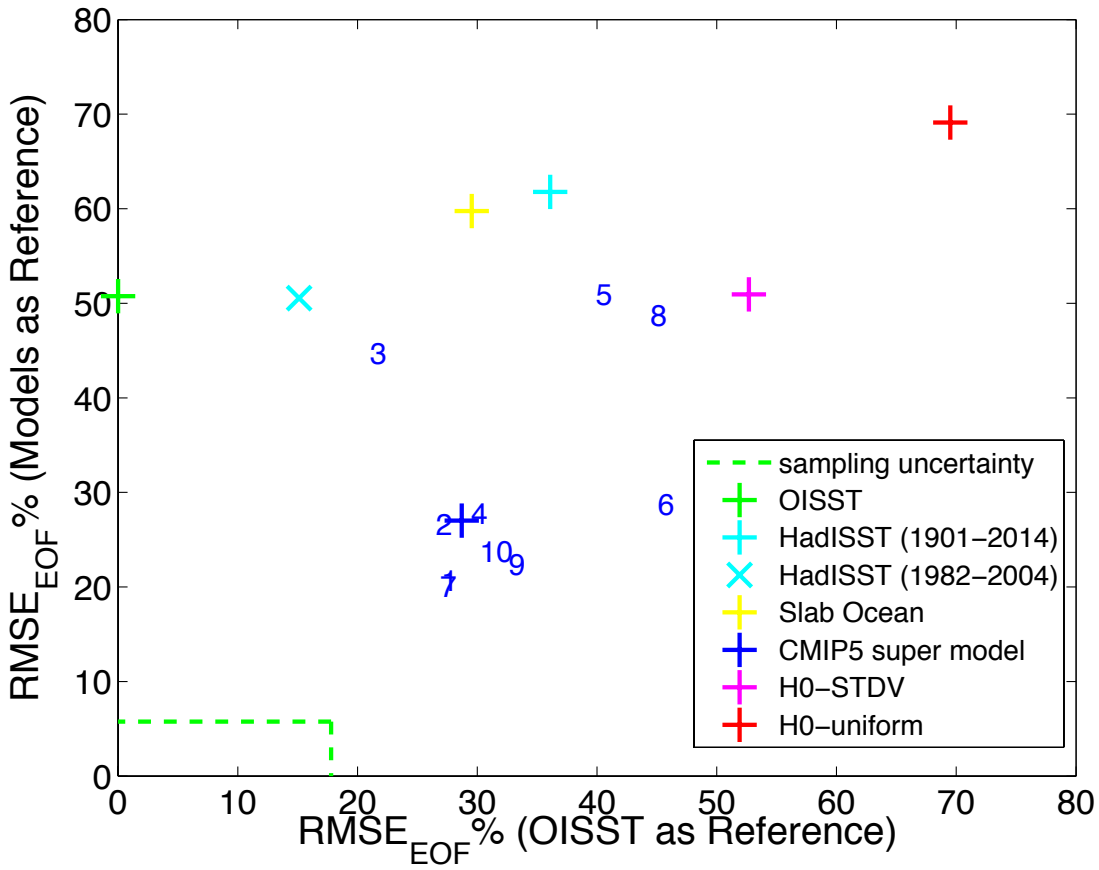

Fig. 2 $RMSE_{EOF}$ values distribution relative to the observations (x axis) and mean $RMSE_{EOF}$ values of pairwise comparisons to all CMIP5 model simulations (y axis) for monthly SSTA EOF-analysis in the Southern Ocean. The sampling uncertainty is based on North et al. (1982) and Wang et al (2015).

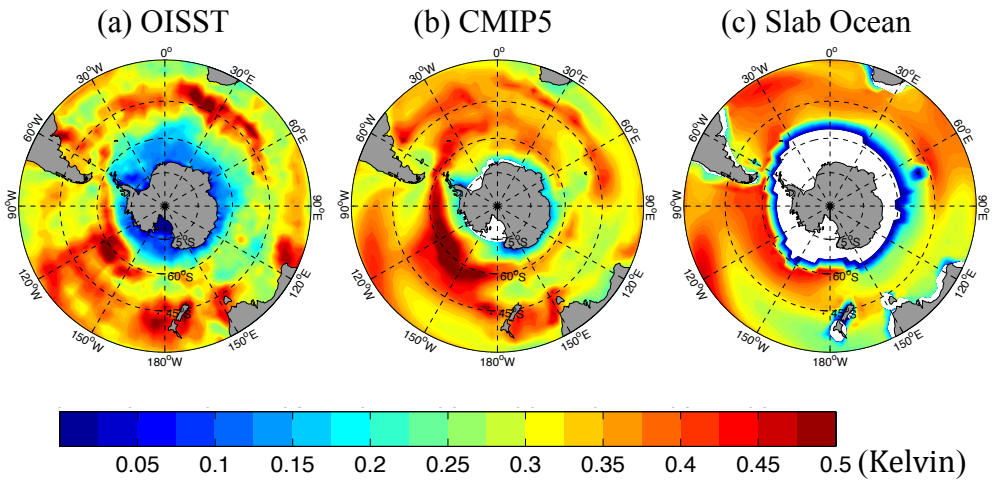

Fig. 3 Standard deviation fields of annual mean SSTA for (a): OISST; (b): CMIP5 super model; (c): Slab Ocean experiment result.

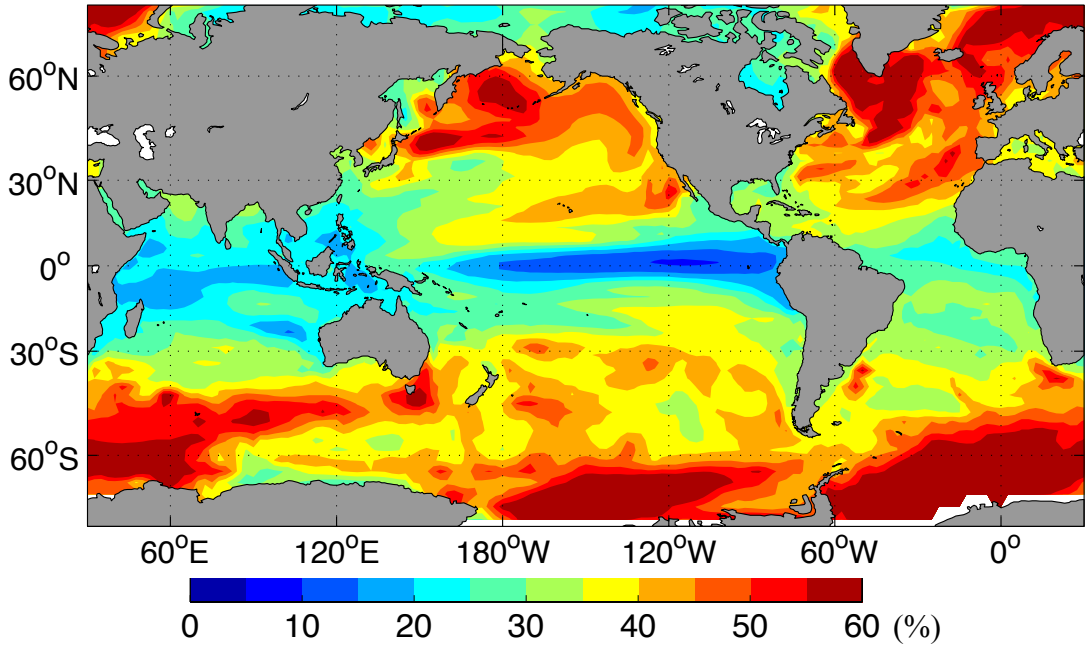

Fig. 4 The relative contribution of Long-term (> 10 years) variability to the total of annual mean variations based on the CMIP5 super model.

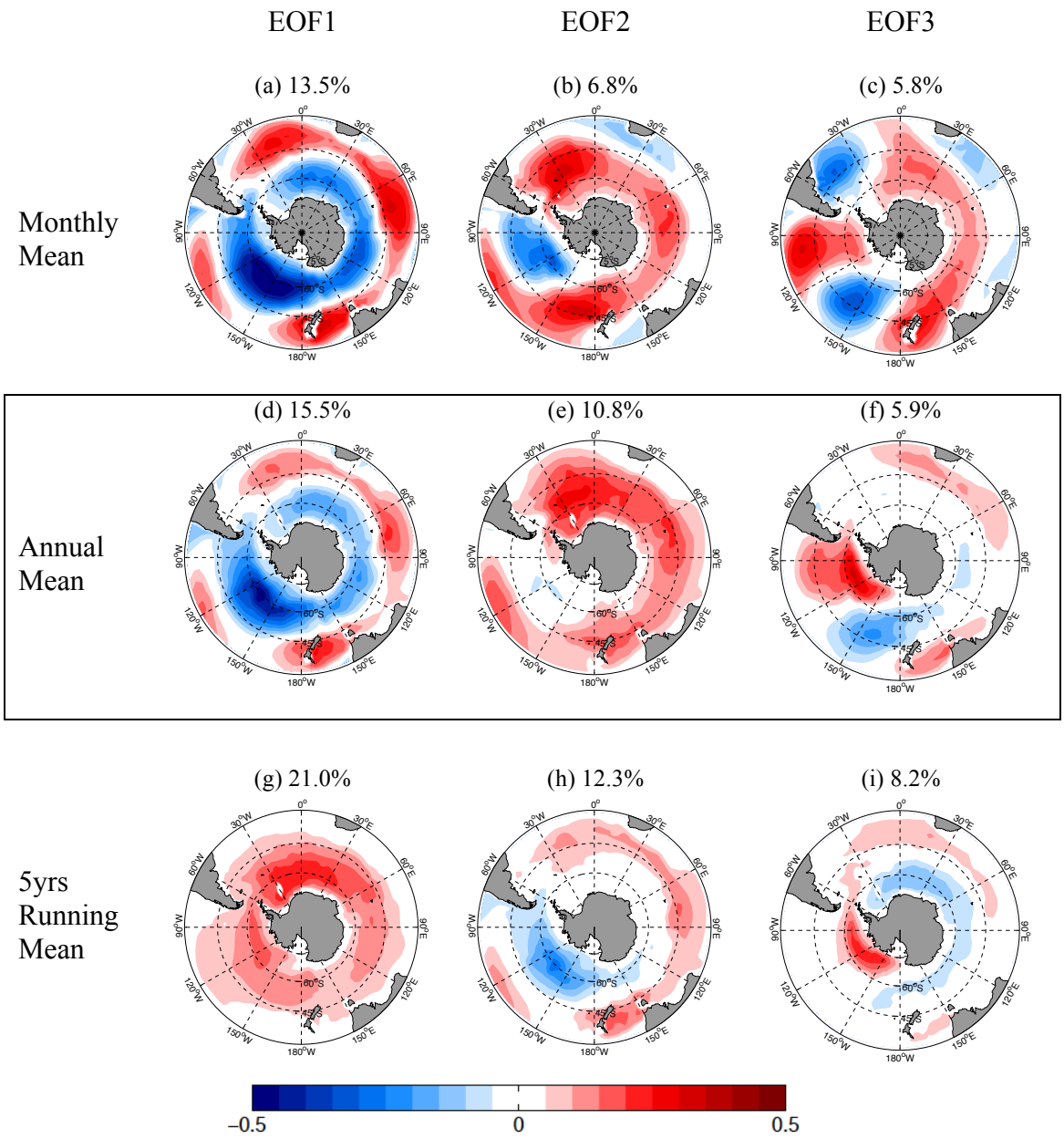

Fig. 5 First three leading EOF patterns of CMIP super model SSTA in the Southern Ocean for (a-c): monthly mean; (d-f): annual mean; (g-i): 5 years running mean. The values in the headings of each panel are the explained variances of each EOF-mode.

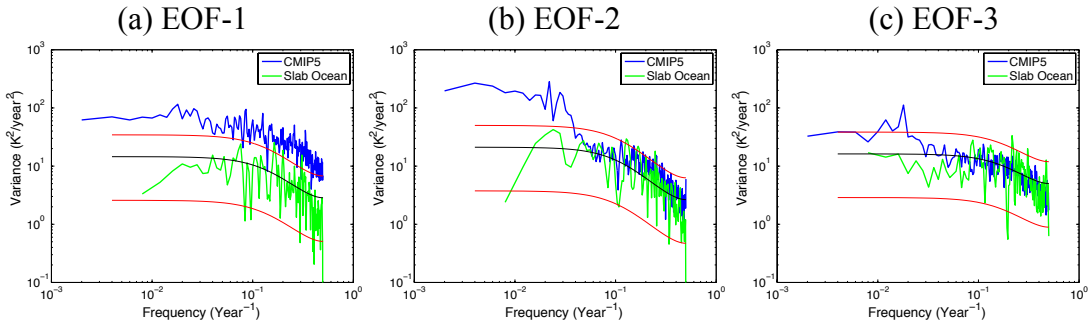

Fig. 6 Spectrum of the time series of the three leading EOF-modes of the CMIP super model annual mean SSTA (as in Fig. 5d-f). The power spectrum of the time series resulting from the projection of these patterns onto the slab ocean simulation SST variability are shown for comparison. The black line is a red noise fit to the slab ocean time series and the red lines mark the 95% confidence interval relative to the red noise fit of the slab ocean simulation.

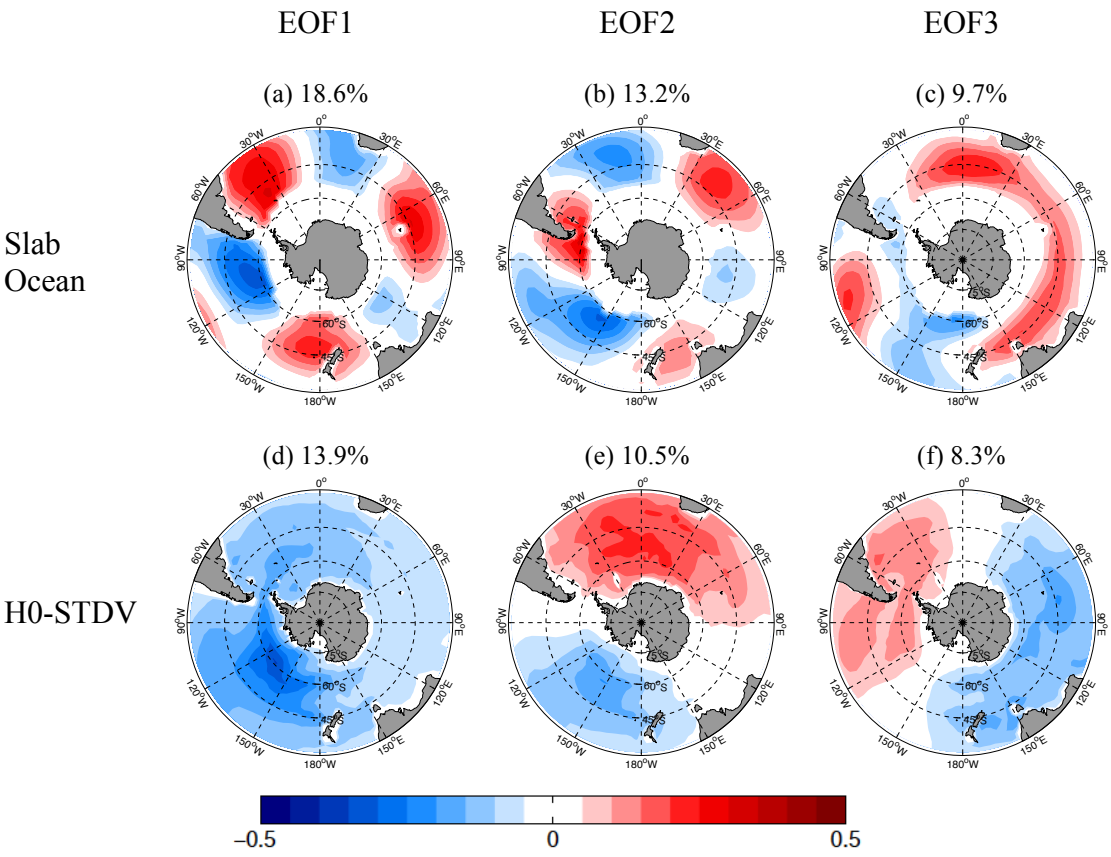

Fig. 7 (a-c): First three leading EOF patterns of detrended annual mean SSTA in the Southern Ocean for (a-c): Slab Ocean; (d-f): H0-STDV null hypothesis. The values in the headings of each panel are the explained variances of each EOF-mode.

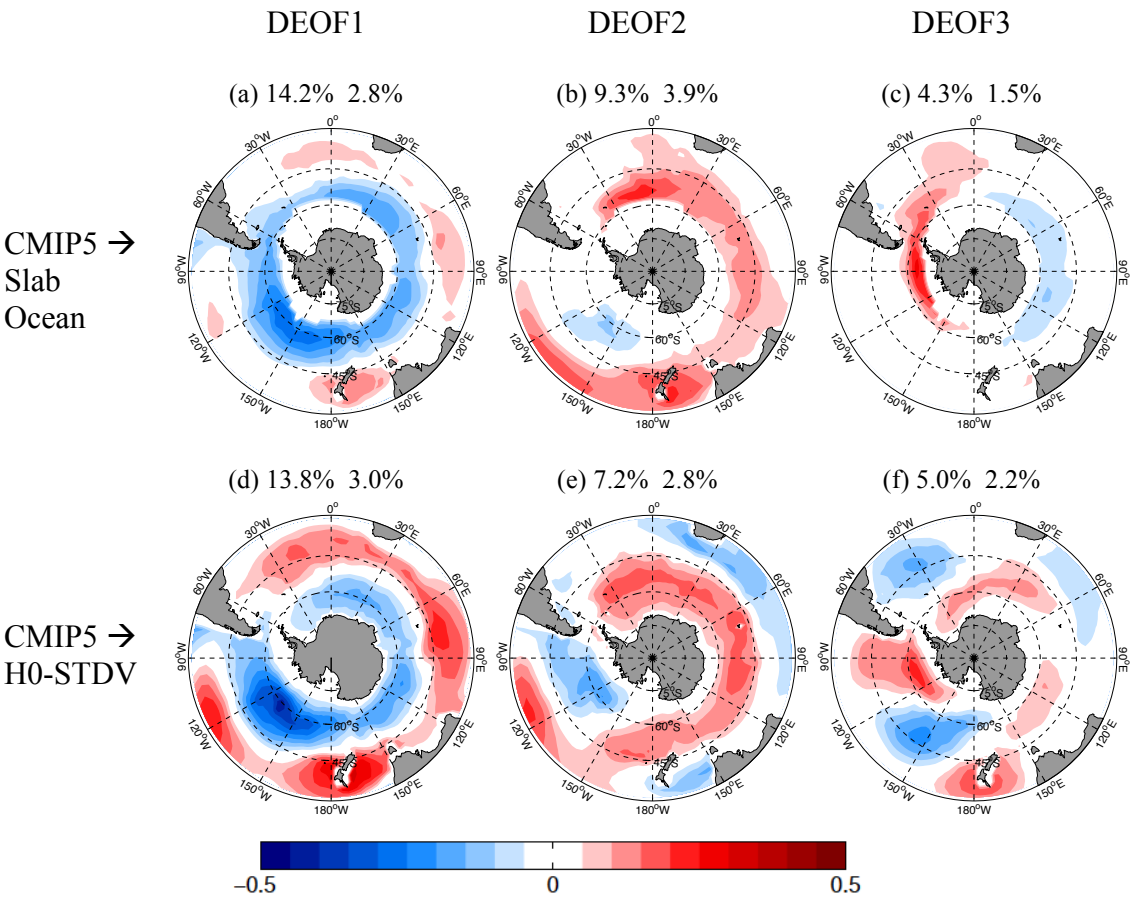

Fig. 8 (a-c): Leading DEOF patterns of annual mean SSTA CMIP5 projection to Slab Ocean; (d-f): Leading DEOF patterns of annual mean SSTA CMIP5 projection to H0-STDV. The headings show the explained variances of the DEOF-modes in the CMIP5 super model (first value) and the slab ocean simulation or H0-stdv null hypothesis (second value), respectively.

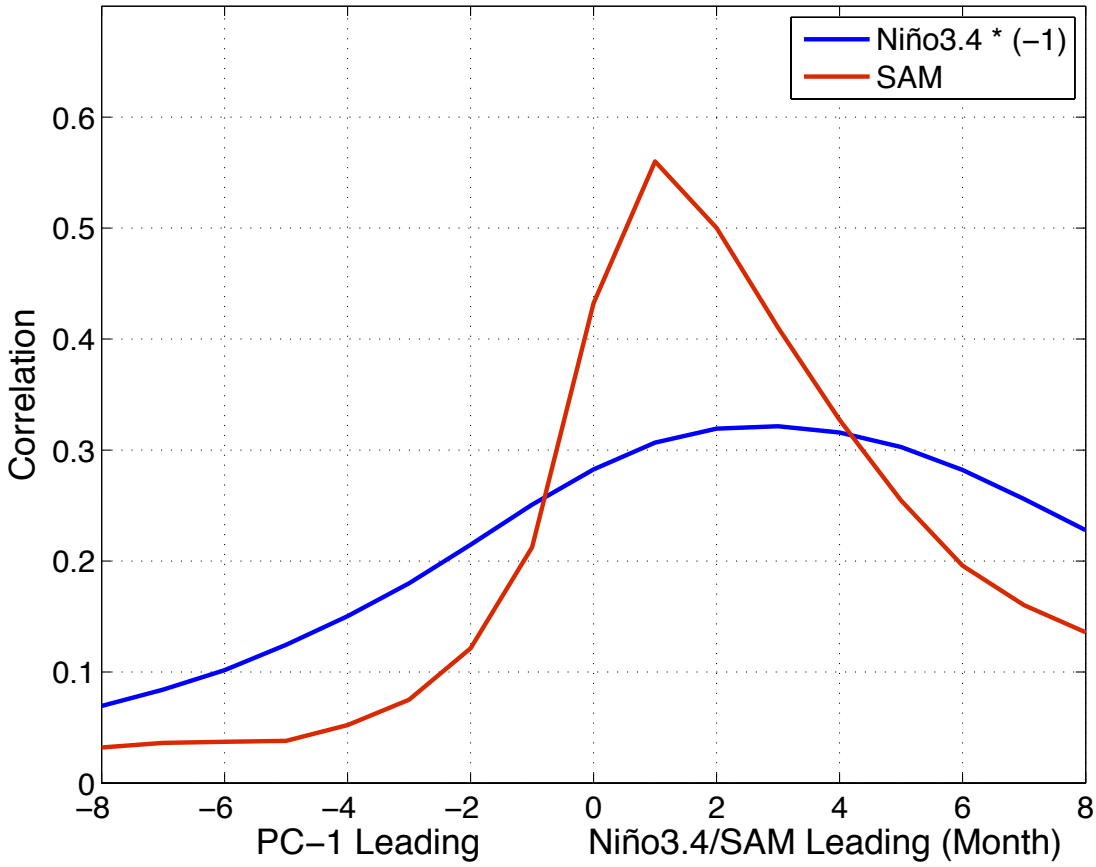

Fig. 9 Lead-lag correlation between Niño3.4/SAM and monthly mean PC-1 time series of CMIP super ensemble. Note that the correlation with Niño3.4 is multiplied by minus one to be positive.

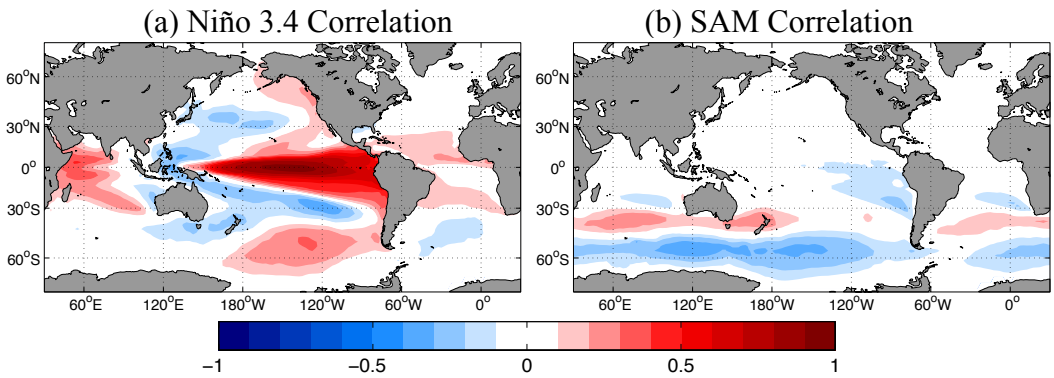

Fig. 10 (a): Monthly SSTA correlation with Niño 3.4 in CMIP5 super model; (b): same as (a) but for the correlation between SSTA and SAM index.

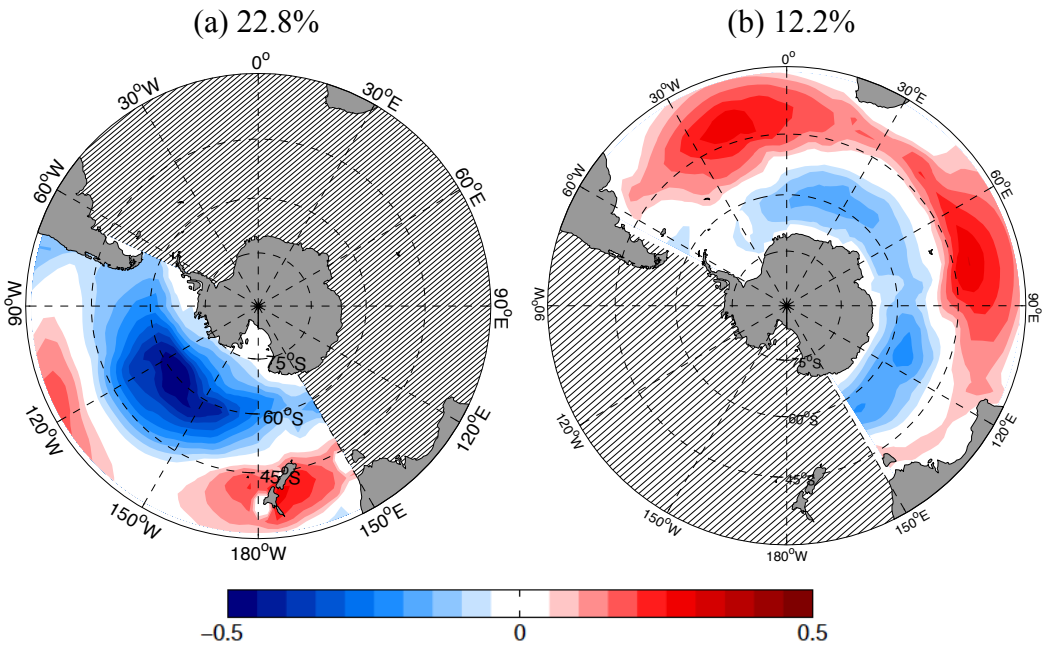

Fig. 11 (a): CMIP5 super model EOF-1 of annual mean SST in South Pacific; (b): EOF-2 of annual mean SST in South Atlantic and Indian Ocean. The values in the headings of each panel are the explained variances of each EOF-mode.

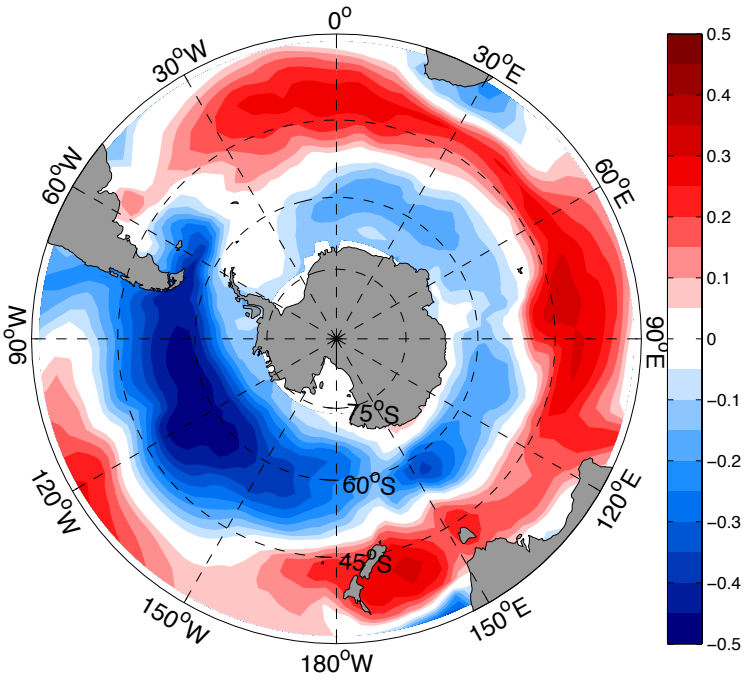

Fig. 12 Correlation between a reconstructed SSTA PC-1 time series and SSTA of the CMIP5 super model on annual time scale. See text for details on the reconstruction model.

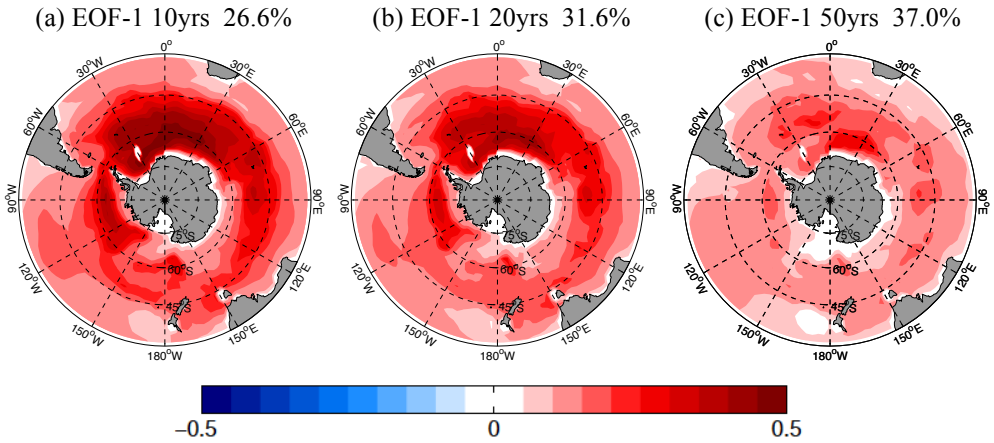

Fig. 13 EOF-1 of SSTA in Southern Ocean of the CMIP5 super ensemble for (a): 10 years running mean; (b) 20 years running mean; (c) 50 years running mean. The values in the headings of each panel are the explained variances of each EOF-mode.

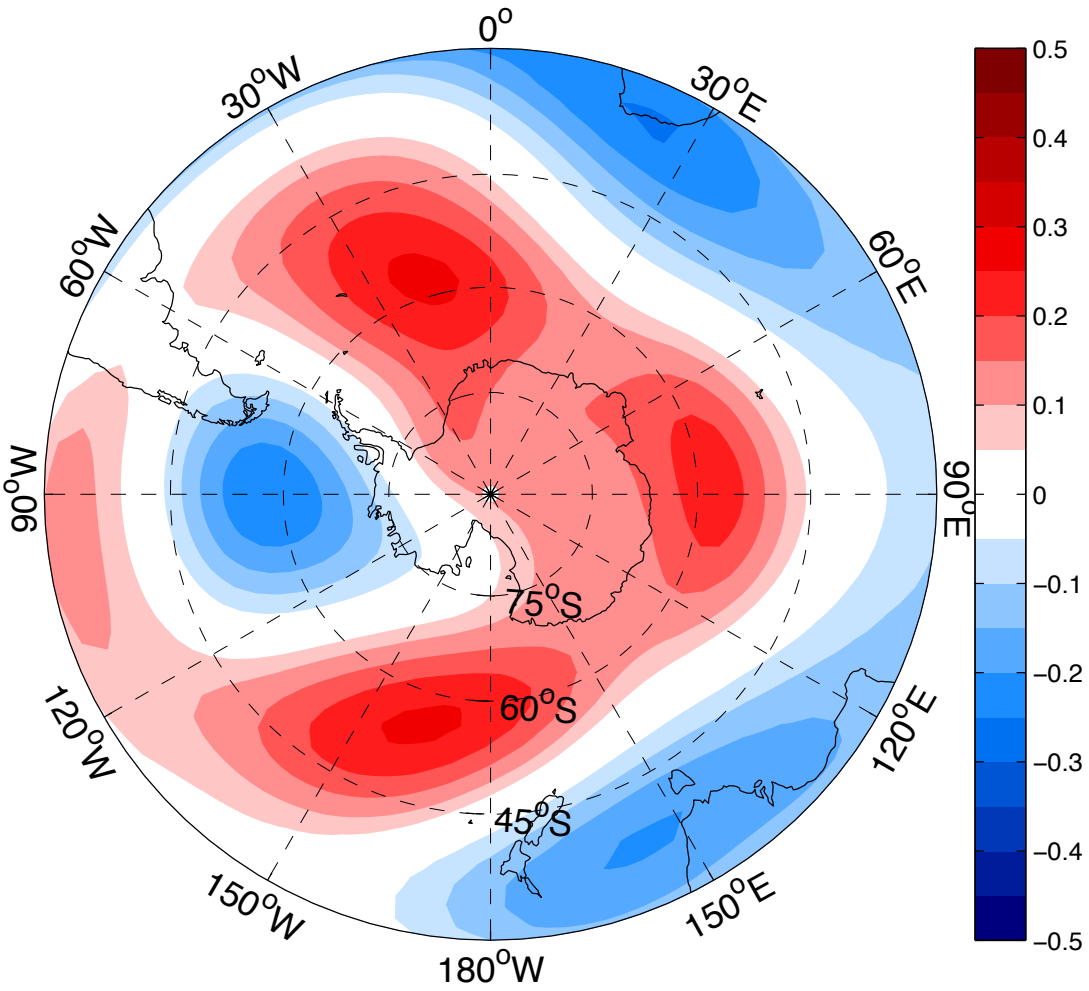

Fig. 14 Correlation between SSTA PC-2 time series and 500hPa geopotential height anomaly of the CMIP5 super model on monthly time scale.

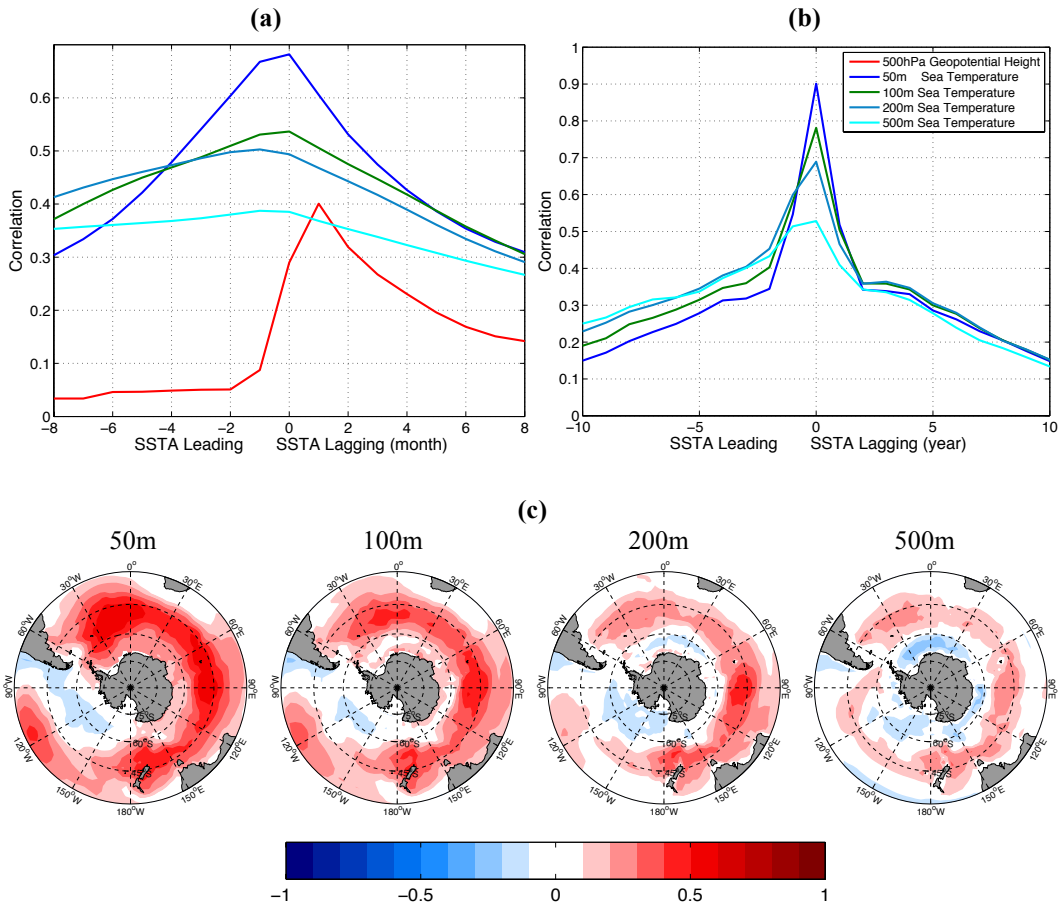

Fig. 15 Lead-lag correlation for box-averaged indices for the monopole mode between SSTA and 500hPa geopotential height/subsurface ocean temperature anomalies. (a): Lead-lag correlation on monthly time scale; (b): same as (a) but for annual time scale; (c): Correlation between SSTA PC-2 time series and subsurface ocean temperature of the CMIP5 super model on annual time scale.

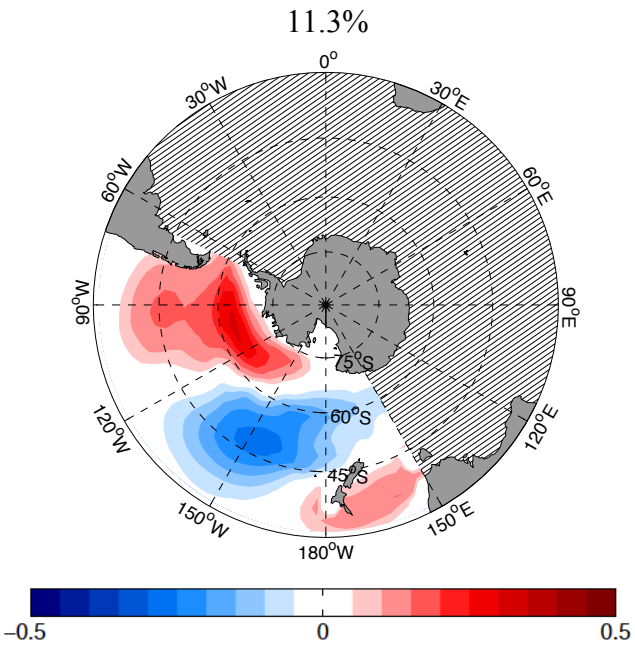

Fig. 16 EOF-2 of CMIP5 super model SST in the South Pacific for annual mean analysis. The value in the heading is the explained variance of this EOF-mode.

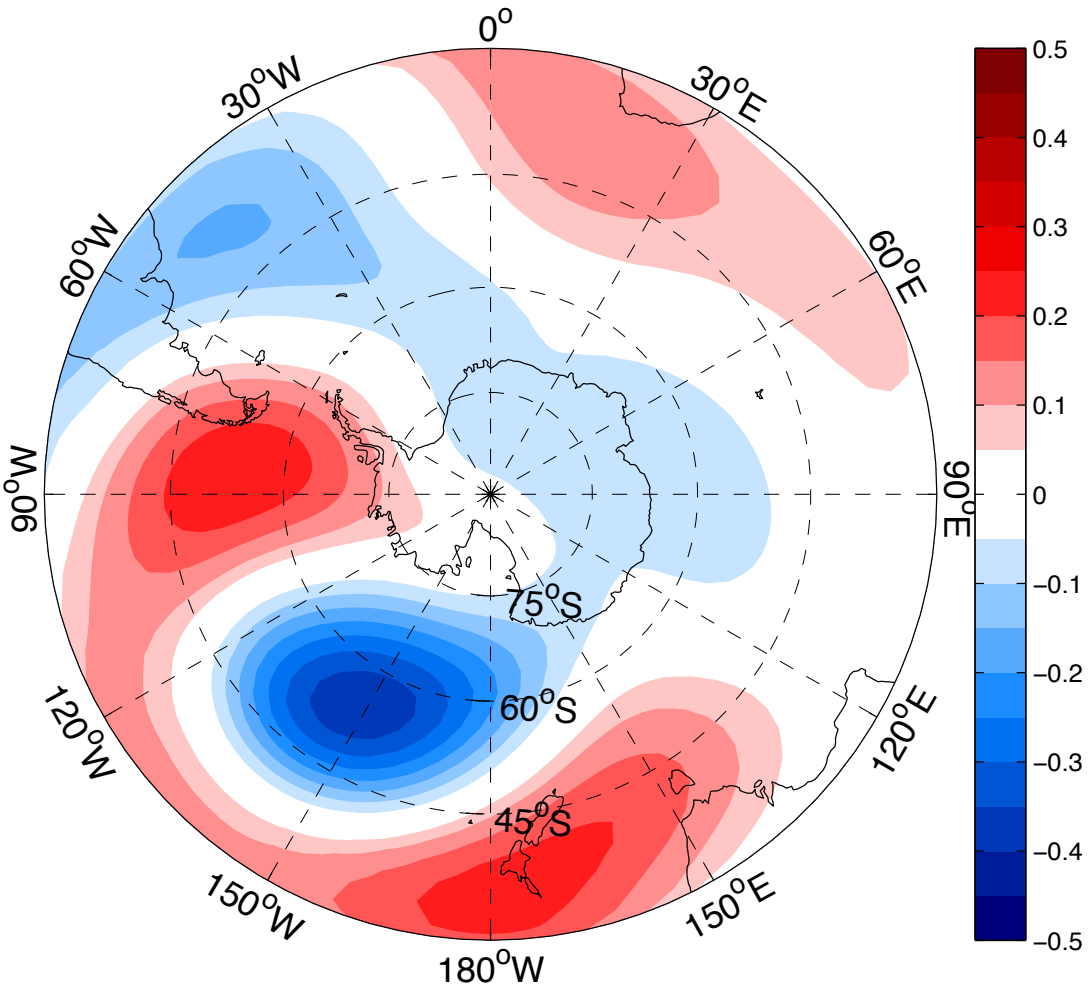

Fig. 17 Correlation between Box [A-B] time series and 500hPa geopotential height anomaly of the CMIP5 super model on monthly time scale.

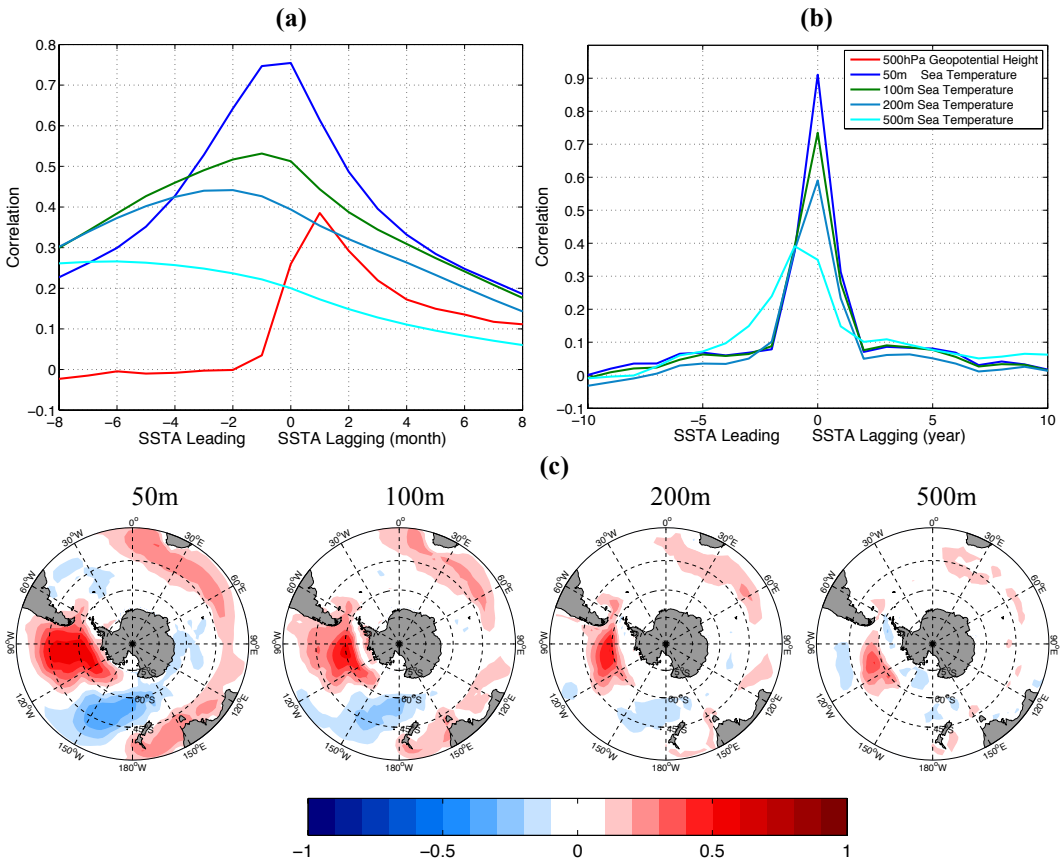

Fig. 18 Lead-lag correlation for $\text{Indices}_{\text{A-B}}$ between SSTA and 500hPa geopotential height/subsurface ocean temperature anomalies. (a): Lead-lag correlation on monthly time scale; (b): same as (a) but for annual time scale; (c): Correlation between SSTA PC-2 time series and subsurface ocean temperature of the CMIP5 super model on annual time scale.

Table .1 List of CMIP5 models

Number	Originating Group(s)	Country	Model
1	CSIRO and BOM	Australia	ACCESS1.0
2	CSIRO and BOM	Australia	ACCESS1.3
3	National Center for Atmospheric Research	USA	CCSM4
4	Canadian Centre for Climate Modelling and Analysis	Canada	CanESM2
5	Geophysical Fluid Dynamics Laboratory	USA	GFDL-CM3
6	Geophysical Fluid Dynamics Laboratory	USA	GFDL-ESM2G
7	Hadley Centre for Climate Prediction and Research / Met Office	UK	HadGEM2-ES
8	Institut Pierre Simon Laplace	France	IPSL-CM5A-LR
9	Meteorological Research Institute	Japan	MRI-CGCM3
10	Beijing Climate Center	China	bcc-csm1-1

Table. 2 Parameters of linear regression model for annual mean EOF-1 time series discussed in the text.

	α (Ocean Memory)	**β (Niño 3.4)**	**γ (SAM)**
Pacific EOF-1	0.42	-0.69	0.19
Southern Ocean EOF-1	0.38	-0.37	0.25
Atlantic-Indian Ocean EOF-2	0.30	-0.06	0.25